Article

Operation of a silicon quantum processor unit cell above one kelvin

https://doi.org/10.1038/s41586-020-2171-6

Received: 19 June 2019

Accepted: 22 January 2020

Check for updates

C. H. Yang[1]✉, R. C. C. Leon[1], J. C. C. Hwang[1,6], A. Saraiva[1], T. Tanttu[1], W. Huang[1], J. Camirand Lemyre[2], K. W. Chan[1], K. Y. Tan[3,7], F. E. Hudson[1], K. M. Itoh[4], A. Morello[1], M. Pioro-Ladrière[2,5], A. Laucht[1] & A. S. Dzurak[1]✉

Quantum computers are expected to outperform conventional computers in several important applications, from molecular simulation to search algorithms, once they can be scaled up to large numbers—typically millions—of quantum bits (qubits)[1–3]. For most solid-state qubit technologies—for example, those using superconducting circuits or semiconductor spins—scaling poses a considerable challenge because every additional qubit increases the heat generated, whereas the cooling power of dilution refrigerators is severely limited at their operating temperature (less than 100 millikelvin)[4–6]. Here we demonstrate the operation of a scalable silicon quantum processor unit cell comprising two qubits confined to quantum dots at about 1.5 kelvin. We achieve this by isolating the quantum dots from the electron reservoir, and then initializing and reading the qubits solely via tunnelling of electrons between the two quantum dots[7–9]. We coherently control the qubits using electrically driven spin resonance[10,11] in isotopically enriched silicon[12] ^{28}Si, attaining single-qubit gate fidelities of 98.6 per cent and a coherence time of 2 microseconds during 'hot' operation, comparable to those of spin qubits in natural silicon at millikelvin temperatures[13–16]. Furthermore, we show that the unit cell can be operated at magnetic fields as low as 0.1 tesla, corresponding to a qubit control frequency of 3.5 gigahertz, where the qubit energy is well below the thermal energy. The unit cell constitutes the core building block of a full-scale silicon quantum computer and satisfies layout constraints required by error-correction architectures[8,17]. Our work indicates that a spin-based quantum computer could be operated at increased temperatures in a simple pumped ^{4}He system (which provides cooling power orders of magnitude higher than that of dilution refrigerators), thus potentially enabling the integration of classical control electronics with the qubit array[18,19].

Q1

Electrostatically gated quantum dots (QDs) in Si/SiGe or Si/SiO_2 heterostructures are prime candidates for spin-based quantum computing owing to their long coherence times, high control fidelities and industrial manufacturability[13,14,20–23]. In large-scale quantum processors, the qubits will be arranged in either one-dimensional chains[17] or two-dimensional arrays[3] to enable quantum error-correction schemes. In architectures relying on exchange coupling for two-qubit operation[15,16,24,25], the QDs are expected to be densely packed. Until now, two-qubit QD systems have been tunnel-coupled to a nearby charge reservoir that has typically been used for initialization and readout using spin-to-charge conversion[26]. Here we demonstrate an isolated double-QD system that requires no tunnel-coupled reservoir[7–9] to perform full two-qubit initialization, control and readout. When combined with gate-dispersive readout[9,27] and compatible qubit control techniques—such as global control inside a microwave cavity[8], a cross-bar microwave antenna array[28] or a nanoscale magnet array—such a double-QD system constitutes the elementary unit cell of a scalable quantum processor (see Fig. 1h).

Figure 1a shows a scanning electron microscope image of a silicon metal–oxide–semiconductor (Si-MOS) double-QD device that is nominally identical to the one measured. The device is designed with a cobalt micromagnet to facilitate electrically driven spin resonance (EDSR), whereby an a.c. voltage at frequency f_{qubit} is applied to the micromagnet electrode to drive the spin resonance[10], and a single-electron transistor (SET) charge sensor is used to detect changes in the electron occupation of the two QDs[11]. The experimental setup is described in Extended Data Fig. 1. In Fig. 1b–f we illustrate the tuning sequence that we use to configure the isolated double-QD unit cell in the (3, 3) charge configuration. We start by accumulating the desired total number of electrons under G_1, then deplete the electrons under gates J and G_2, and finally cut off

Q2 Q3 Q4 Q5

[1]Centre for Quantum Computation and Communication Technology, School of Electrical Engineering and Telecommunications, University of New South Wales, Sydney, New South Wales, Australia. [2]Institut Quantique et Département de Physique, Université de Sherbrooke, Sherbrooke, Québec, Canada. [3]QCD Labs, QTF Centre of Excellence, Department of Applied Physics, Aalto University, Aalto, Finland. [4]School of Fundamental Science and Technology, Keio University, Yokohama, Japan. [5]Quantum Information Science Program, Canadian Institute for Advanced Research, Toronto, Ontario, Canada. [6]Present address: Research and Prototype Foundry, The University of Sydney, Sydney, New South Wales, Australia. [7]Present address: IQM Finland Oy, Espoo, Finland. ✉e-mail: henry.yang@unsw.edu.au; a.dzurak@unsw.edu.au

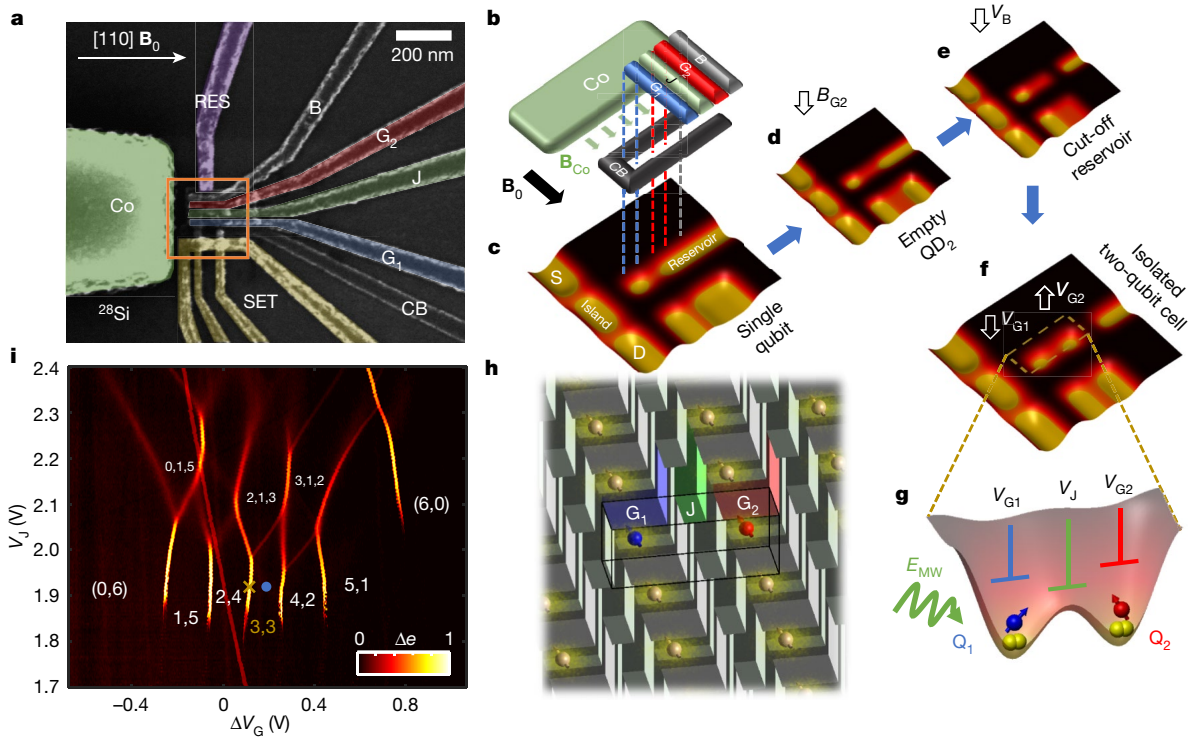

Fig. 1 | An isolated spin qubit processor unit cell. a, Scanning electron microscope image of a two-qubit device identical to the one used in the experiments with a Co micromagnet for EDSR control[11]. RES, electron reservoir; B, barrier gate; CB, confinement barrier gate. **b**, Schematic of the Al gate stack. QDs are defined under G_1 and G_2 and laterally confined by CB. Gate J controls the coupling between the QDs, and B can be biased to create a barrier between the QDs and the electron reservoir. The Co micromagnet provides a magnetic field gradient while simultaneously delivering a microwave voltage signal to enable EDSR. The charge sensor (SET) and electron reservoir are not shown in this schematic. **c**–**f**, Tuning sequence used to obtain an isolated (3, 3) electron configuration. Starting with a single dot under G_1 as in ref. [11], we load six electrons from the reservoir onto QD1 (**c**). We lower the voltage of G_2, V_{G2}, just enough to deplete all electrons under G_2 (**d**) and reduce V_B from 3.2 V to 0 V to create a barrier that makes it almost impossible for electrons to escape (**e**). We re-bias V_{G1} and V_{G2} to define QD_2 under G_2, and move three electrons from QD_1 to QD_2 (**f**). **g**, Schematic of the conduction band and control electrodes of the isolated qubit unit cell in the (3, 3) charge configuration. Electron spins in excited valley states are used for qubit operation. **h**, Schematic of a qubit unit cell within a large-scale two-dimensional quantum processor. The unit cell occupies the minimum footprint for operating a two-qubit system. Scaling towards pairwise unit-cell operation allows construction of a complete quantum computer. **i**, Charge stability diagram of the isolated QDs, with a total of six electrons trapped in the system. Δe is the electron charge differential converted from the SET lock-in current. Here, $\Delta V_G = V_{G1} - V_{G2}$ and $V_{G1} + V_{G2} = 4.8$ V. The system evolves into a strongly coupled three-dot system for very positive biasing of V_J. A typical readout position (yellow cross) and control point (blue dot) are labelled in the (3, 3) region. The charge transition near $\Delta V_G = 0$ V is not coupled to the QDs and most probably corresponds to charge movement outside the CB confinement area. Tilting the double-QD potential at low V_J ($V_J < 2$ V) allows us to set any charge configuration between (0, 6) and (6, 0), whereas a high V_J ($V_J > 2$ V) transforms the double-QD system into a triple-QD system, with a third dot forming under gate J.

the electron reservoir by lowering the bias applied to the barrier gate B. At the end of the tuning sequence, the strong barrier confinement ensures that no electrons can tunnel into or out of the qubit cell. The ability to operate the unit cell without any changes in electron occupation throughout initialization, control and readout is a main prerequisite for scaling it up to large two-dimensional arrays (see Fig. 1h), where qubit control can be achieved by global magnetic resonance or via an array of micromagnets that allow local EDSR. Using gates G_1, J and G_2 (see Fig. 1g), we can distribute the six electrons arbitrarily within the qubit cell, as demonstrated in the stability diagram shown in Fig. 1i. We focus on the (3, 3) charge configuration (see Extended Data Fig. 2). Here, the lower two electrons in each dot form a spin-zero closed shell in the lower conduction band valley state, and we use the spins of the unpaired electrons in the upper valley states of the silicon QDs as our qubits[29]. It is also possible to operate the qubits in the (1, 1) and (1, 3) charge configurations (see Extended Data Fig. 3), but (3, 3) is chosen for better EDSR driving strength and J gate control[11].

We depict the entire control, measurement and initialization cycle in Fig. 2a, b. Throughout operation, the same six electrons stay within the unit cell. We measure the two-spin state using a variation of the Pauli spin blockade. As for traditional singlet–triplet readout[30], tunnelling of the electrons into the same dot is allowed only for a spin singlet state owing to the Pauli exclusion principle. On the other hand, not all triplets are blockaded—the T_0 triplet mixes with the singlet state at a rate faster than our SET charge readout. Therefore, any combination of $|\uparrow\downarrow\rangle$ and $|\downarrow\uparrow\rangle$ will be allowed to tunnel. As a result, spin-to-charge conversion in our device manifests itself as spin parity readout, measuring the $\hat{\sigma}_{ZZ}$ projection of the two-qubit system, where $\hat{\sigma}$ is the Pauli operator (see Methods). In the remainder of the paper, we denote this parity readout output as P_{ZZ}, the expectation value of $\hat{P}_{ZZ} = \frac{1}{2}(\hat{\sigma}_{II} - \hat{\sigma}_{ZZ})$, where $\hat{\sigma}_{II}$ is the identity matrix. An even spin state then leads to $P_{ZZ} = 0$ and an odd state leads to $P_{ZZ} = 1$.

Initialization is performed by first preparing the unit cell in the (2, 4) S state, before moving one electron to qubit 1 (Q_1) to create a (3, 3) S-like state. For $hf_{qubit} \gg k_B T$ (h, Planck constant; k_B, Boltzmann constant; T, temperature), we can also initialize the system in the well defined $|\downarrow\downarrow\rangle$ state by dwelling at a spin relaxation hot-spot[15,25]. In Fig. 2c we show Rabi oscillations for the two different initialization states, starting in either the S-like state or the $|\downarrow\downarrow\rangle$ state. Additional verification of the initialized states is performed by spin-relaxation measurements described in Methods and Extended Data Fig. 4.

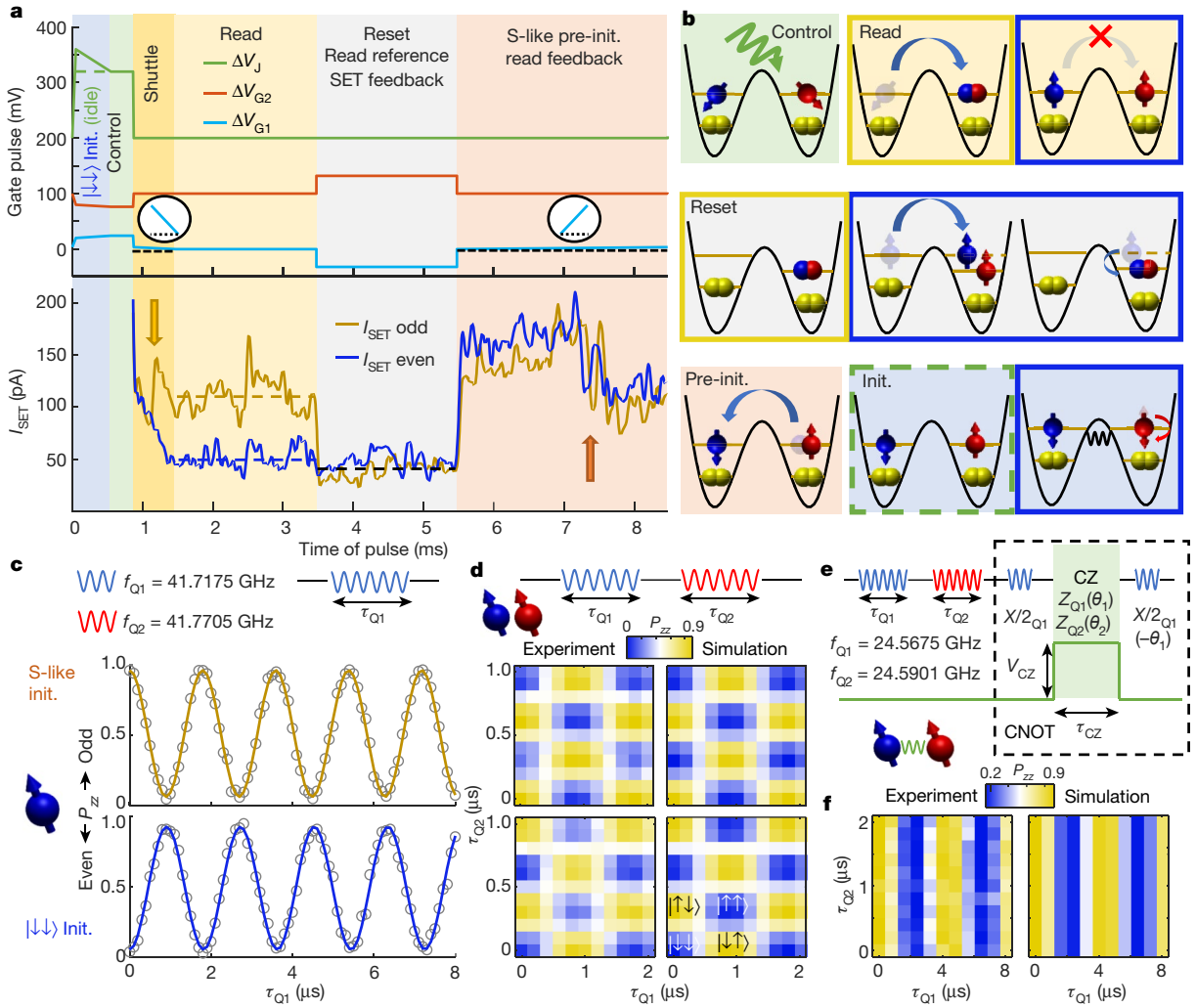

Fig. 2 | Full two-qubit operation in an isolated quantum processor unit cell. **a**, **b**, Operational sequence for two-qubit control, readout, reset, calibration and initialization ('Init.') using single-shot parity readout without any nearby reservoir. Gate pulses and SET current are displayed in **a**, and the corresponding charge movement is depicted in **b**. After the qubit control stage, parity readout (which is based on Pauli spin blockade when trying to shuttle the electron from Q_1 to Q_2) is conducted. In the schematics, the blue sphere represents the electron carrying spin information for Q_1, the red sphere represents the electron carrying spin information for Q_2 and the yellow spheres represent pairs of electrons that form 'inert' spin-zero singlet states within the dots. If blockade occurs, there is no charge movement and the SET current I_{SET} is lower (blue curve, bottom graph in **a**), whereas a higher I_{SET} (yellow curve) is observed when the electron is not blockaded. The reset stage forces the blue electron to move to Q_2 regardless of its spin state, by pulsing deep enough to overcome the Pauli spin blockade. The system subsequently relaxes into the (2, 4) S state. The current I_{SET} measured here is used as reference for the parity readout. Next, the blue electron is moved back to Q_1, resulting in an S-like state being initialized. Finally, the system can be left in the S-like state (odd-parity spin) or initialized in the T_- state ($|\downarrow\downarrow\rangle$) if pulsed to a hot-spot relaxation region before control. **c**, Rabi oscillations of Q_1 with initialization in the S-like (top panel) and $|\downarrow\downarrow\rangle$ (bottom panel) states. During parity readout (P_{ZZ}), even parity is mapped to low signal (0) and odd parity to high signal (1). The fitted Rabi oscillation amplitude is about 90%. Data measured at 40 mK and 1.4 T. **d**, Serially driven Rabi rotations on two independent (uncoupled) qubits and subsequent parity readout for S-like (top panel) and $|\downarrow\downarrow\rangle$ (bottom panel) initialization. For $|\downarrow\downarrow\rangle$ initialization, the oscillations span the separable two-qubit space with $|\downarrow\downarrow\rangle$ and $|\uparrow\uparrow\rangle$, giving a low signal, and with $|\downarrow\uparrow\rangle$ and $|\uparrow\downarrow\rangle$, giving a high signal. The simulations (right panels) further validate that the parity readout does indeed follow the expectation value of the $\hat{P}_{ZZ} = \frac{1}{2}(\hat{\sigma}_{II} - \hat{\sigma}_{ZZ})$ projection. Data measured at 40 mK and 1.4 T. **e**, Sequence used to implement a CNOT two-qubit logic gate via a CZ rotation using control of gate J. The final π/2 pulse incorporates a phase shift to compensate the Stark shift from pulsing gate J. **f**, Applying a CNOT gate before readout turns the parity readout into single-qubit spin readout. Starting with $|\downarrow\downarrow\rangle$ initialization, when the CNOT gate is applied after the serial two-qubit Rabi oscillations from **d**, we measure only the Rabi oscillations of Q_1. Tiny oscillations (period, 1 μs) in the experimental data (left panel) along the *y* direction can still be observed owing to imperfect CZ pulsing. Simulations are shown in the right panel. Data measured at 40 mK and 0.8 T. Here, $X/2_{Q1}$ is a π/2 rotation about the *X* axis for Q_1, $Z_{Q1,2}$ is a rotation about the *Z* axis for $Q_{1,2}$, $\theta_{1,2}$ is the phase offset (*Z* rotation) of $Q_{1,2}$, and $\tau_{Q1,2}$ is the microwave pulse time for $Q_{1,2}$.

We confirm that our readout procedure distinguishes the state parity by serially driven Rabi rotations shown in Fig. 2d, where we coherently and unconditionally rotate first Q_1 and then Q_2, and measure the output state. Reading all other two-qubit projections, and therefore being able to measure the full two-qubit space, is also straightforward. By rotating one of the qubits by π/2 we gain access to $\hat{P}_{ij} = \frac{1}{2}(\hat{\sigma}_{II} - \hat{\sigma}_{ij})$, where $i, j \in \{X, Y, Z\}$. Furthermore, by adding a conditional two-qubit gate—such as a CNOT—before readout, we can turn the parity readout into a single-qubit readout. Figure 2e shows the pulse sequence from Fig. 2d with an added CNOT gate based on performing a conditional *Z* (CZ) gate. We achieve the conditional phase shift by pulsing gate J to temporarily increase the coupling (*J*) between the two qubits (without changing the charge detuning). The single-qubit readout result is shown in Fig. 2f. The sequence reads out only the Q_1 spin state as $\hat{P}_{Z1} = \frac{1}{2}(\hat{\sigma}_{II} - \hat{\sigma}_{ZI})$,

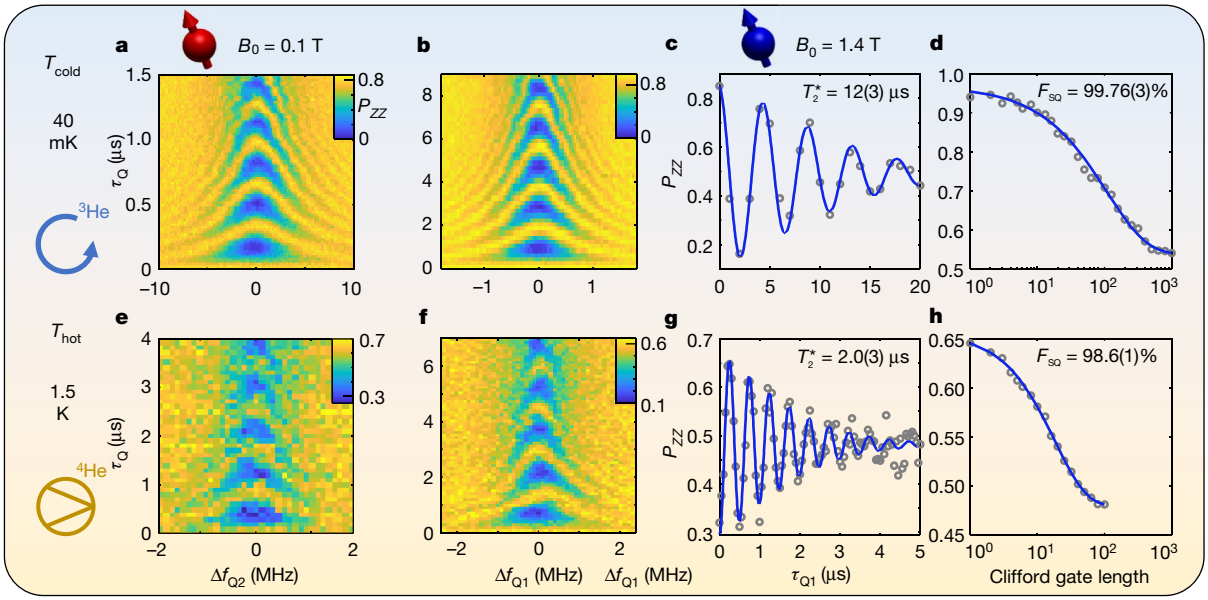

Fig. 3 | Qubit operation at high temperature and low magnetic field. **a**–**d**, ^{3}He circulation is on, with mixing chamber temperature of T_{cold} = 40 mK. **a**, Rabi chevron of Q_2 at B_0 = 0.1 T, where f_{Q2} = 3.529 GHz. **b**, Rabi chevron of Q_1 at B_0 = 1.4 T, where f_{Q1} = 41.71 GHz. **c**, Ramsey coherence time, T_2^*, at B_0 = 1.4 T. **d**, Randomized benchmarking performance at B_0 = 1.4 T. Each data point is the average of 102 randomized sequences with 100 single shots each. **e**–**h**, Pumped ^{4}He only, with T_{hot} = 1.5 K. **e**, Rabi chevron of Q_2 at B_0 = 0.1 T, where f_{Q2} = 3.535 GHz, and $hf_{Q2} \ll k_BT$ = 125 μeV. **f**, Rabi chevron of Q_1 at B_0 = 1.4 T, where f_{Q1} = 41.71 GHz. **g**, Ramsey coherence time, T_2^*, at B_0 = 1.4 T. **h**, Randomized benchmarking performance at B_0 = 1.4 T. Each data point is the average of 280 randomized sequences with 100 single shots each. The drop in visibility can be attributed to a lower charge readout fidelity owing to the broadening of the SET peak (see Extended Data Fig. 9). The error range of the benchmark numbers is within 95% confidence level. See Methods for the details and setup of the Ramsey measurements. The randomized benchmarking protocol is identical to the one used in ref. [20], with expanded data shown in Extended Data Fig. 10.

independently of Q_2. To read out Q_2, one would simply need to swap the target and the control of the CNOT gate. The small but visible oscillations along the *y* axis in the data are due to imperfect CZ pulsing. Details of the CNOT gate data are shown in Extended Data Fig. 5, where the CNOT gate parameters in panel Extended Data Fig. 5c are the same as those for Fig. 2f.

Having demonstrated the general operation of the quantum processor unit cell, including initialization, one- and two-qubit control, and parity and single-qubit readout, we can now investigate the effect of the temperature. For large-scale quantum computer integration, the benefits of raising the temperature to reduce engineering constraints must be carefully balanced with the presence of increased noise. Prior studies have examined the relaxation of Si-MOS QD spin qubits at temperatures of 1.1 K (ref. [31]) and the coherence times of ensembles of Si-MOS QDs up to 10 K (ref. [32]). The coherence times of single deep-level impurities in silicon at 10 K (ref. [33]) and ensembles of donor electron spins in silicon up to 20 K (refs. [34,35]) have also been examined. However, gate fidelities of these qubits have not been investigated yet. Here we investigate the gate fidelity of a fully controllable spin qubit at 1.5 K.

In Fig. 3 we present single-qubit Rabi chevrons and randomized benchmarking for temperatures of T_{cold} = 40 ± 5 mK in Fig. 3a–d, and T_{hot} = 1.5 ± 0.1 K in Fig. 3e–h (the uncertainties denote the fluctuation of the temperature reading over time). Here, T_{hot} = 1.5 K is achieved by simply pumping on the ^{4}He in the 1-K pot of the dilution refrigerator while the ^{3}He circulation is completely shut off. Qubit operation and readout at this increased temperature is possible because our QDs have relatively high valley splitting (>500 μeV) and orbital splitting energies (>2.5 meV)[11]. We observe Rabi chevrons, indicating coherent qubit control, for external magnetic fields of B_0 = 1.4 T and B_0 = 0.1 T at T_{hot} = 1.5 K, in a regime in which the thermal energy is larger than the qubit energy ($k_BT \gg hf_{qubit}$).

We then focus on a performance comparison between different temperatures at B_0 = 1.4 T. From the decay of the Ramsey oscillations in Fig. 3g we determine at this increased temperature a coherence time of $T_2^* = 2.0 \pm 0.3$ μs, which is comparable to that in natural silicon at millikelvin temperatures[13–16]. The single-qubit gate fidelity extracted from randomized benchmarking is F_{SQ} = (98.6 ± 0.1)%, nearly at the fault-tolerance level (see Fig. 3h). For reference, the qubit's performance at T_{cold} = 40 mK is shown in Fig. 3a–d, where both T_2^* and F_{SQ} are about six times better. The similar scaling factors for T_2^* and F_{SQ} indicate that our gate fidelities are predominantly limited by the coherence times of the qubit.

We present a more detailed study of the coherence times and relaxation times as a function of mixing chamber temperature T_{MC} in Fig. 4. A similar study as a function of external magnetic field is presented in Extended Data Fig. 8, where we observe the Hahn echo time, T_2^{Hahn}, to scale linearly with B_0, where shorter relaxation times at lower field are possibly due to spin–orbit Johnson noise[36]. Temperature has the strongest impact on T_1, which scales as T^{-5} between 0.5 K and 1.0 K. This could be interpreted as a Raman process involving intervalley piezophonons stemming from the oxide layer; if the spin–lattice relaxation was dominated by Si deformation potential phonons, the temperature power law should be stronger, as discussed in ref. [31]. T_2^{Hahn} and T_2^* display a weaker dependence on temperature.

The results in Fig. 4 show a substantial reduction in spin relaxation and coherence times going from 100 mK to 1.5 K. Although this reduction does not prevent the qubits from being operated at this temperature, future device engineering should aim to minimize possible sources of noise for optimized high-temperature operation. Residual ^{29}Si nuclear spins that couple to the qubits through the hyperfine interaction lead to background magnetic field noise that could be easily reduced by using silicon substrates with higher isotopic enrichment[37]. Our devices contain 800 ppm residual ^{29}Si atoms, which is more than one order of magnitude higher than what is currently available[12,35]. Although the gradient magnetic field from a micromagnet, as required for EDSR operation[10,11,14], might freeze out nuclear spin dynamics[35],

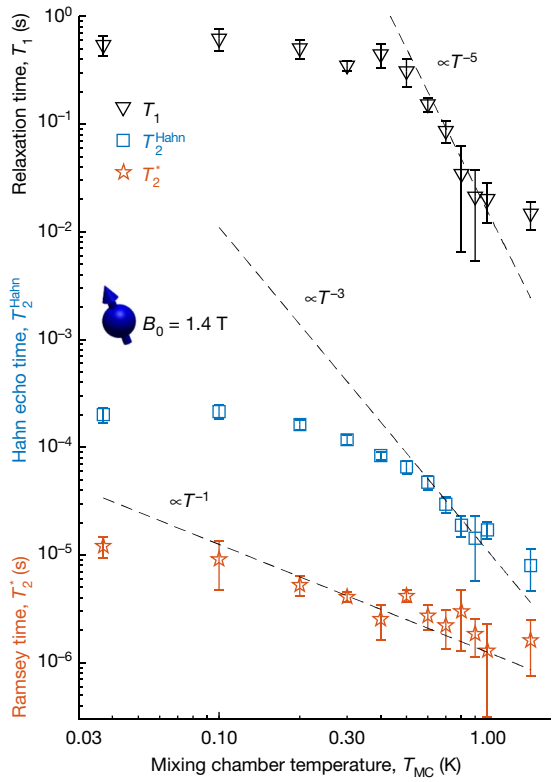

Fig. 4 | Temperature dependence of qubit properties. Spin relaxation time, T_1, Hahn echo coherence time, T_2^{Hahn}, and Ramsey coherence time, T_2^* of Q_1 as a function of mixing chamber temperature at $B_0 = 1.4$ T. The dotted lines indicate trends of $\propto T^{-5}$ for T_1, $\propto T^{-3}$ for T_2^{Hahn}, and $\propto T^{-1}$ for T_2^*. Error bars represent the 95% confidence level.

it will also make the qubits more sensitive to electric field noise induced by the artificial spin–orbit coupling[36]. Charge noise has been shown to increase with temperature[31], and could constitute the dominant noise source for EDSR systems at increased temperatures. Furthermore, because the drop in visibility in Fig. 3 can be attributed to a lower charge readout fidelity owing to the broadening of the SET peak (see Extended Data Fig. 9), replacing the SET current readout with a readout mechanism that offers better signal-to-noise ratios should improve readout fidelities at higher temperatures, as recently demonstrated in ref. [38]. Radio-frequency gate-dispersive readout[9,27,38] could act as a solution and simultaneously provide a truly scalable unit-cell footprint.

In conclusion, we have presented a fully operable two-qubit system in an isolated quantum processor unit cell that allows operation up to 1.5 K—a temperature that is conveniently achieved using pumped ^{4}He cryostats—in which we reach near fault-tolerant single-qubit fidelities. These results pave the way for scaling of silicon-based quantum processors to very large numbers of qubits. Thermal effects on multi-qubit entangled states and the robustness of quantum error correction methods at increased temperature are important questions that need to be explored in future studies of large-scale quantum computer systems.

Online content

Any methods, additional references, Nature Research reporting summaries, source data, extended data, supplementary information, acknowledgements, peer review information; details of author contributions and competing interests; and statements of data and code availability are available at https://doi.org/10.1038/s41586-020-2171-6.

1. Feynman, R. P. Simulating physics with computers. *Int. J. Theor. Phys.* **21**, 467–488 (1982).
2. Loss, D. & DiVincenzo, D. P. Quantum computation with quantum dots. *Phys. Rev. A* **57**, 120–126 (1998).
3. Fowler, A. G., Mariantoni, M., Martinis, J. M. & Cleland, A. N. Surface codes: towards practical large-scale quantum computation. *Phys. Rev. A* **86**, 032324 (2012).
4. Devoret, M. H., Wallraff, A. & Martinis, J. M. Superconducting qubits: a short review. Preprint at https://arxiv.org/abs/cond-mat/0411174 (2004).
5. Vandersypen, L. et al. Interfacing spin qubits in quantum dots and donors—hot, dense, and coherent. *npj Quant. Inf.* **3**, 34 (2017).
6. Almudever, C. G. et al. The engineering challenges in quantum computing. In *2017 Design, Automation & Test in Europe Conference & Exhibition (DATE)*, 836–845 (IEEE, 2017).
7. Bertrand, B. et al. Quantum manipulation of two-electron spin states in isolated double quantum dots. *Phys. Rev. Lett.* **115**, 096801 (2015).
8. Veldhorst, M., Eenink, H. G. J., Yang, C. H. & Dzurak, A. S. Silicon CMOS architecture for a spin-based quantum computer. *Nat. Commun.* **8**, 1766 (2017).
9. Crippa, A. et al. Gate-reflectometry dispersive readout and coherent control of a spin qubit in silicon. *Nat. Commun.* **10**, 2776 (2019).
10. Pioro-Ladrière, M. et al. Electrically driven single-electron spin resonance in a slanting Zeeman field. *Nat. Phys.* **4**, 776 (2008).
11. Leon, R. C. C. et al. Coherent spin control of *s*-, *p*-, *d*- and *f*-electrons in a silicon quantum dot. *Nat. Commun.* **11**, 797 (2020).
12. Itoh, K. M. & Watanabe, H. Isotope engineering of silicon and diamond for quantum computing and sensing applications. *MRS Commun.* **4**, 143–157 (2014).
13. Takeda, K. et al. A fault-tolerant addressable spin qubit in a natural silicon quantum dot. *Sci. Adv.* **2**, e1600694 (2016).
14. Kawakami, E. et al. Gate fidelity and coherence of an electron spin in an Si/SiGe quantum dot with micromagnet. *Proc. Natl Acad. Sci. USA* **113**, 11738–11743 (2016).
15. Watson, T. F. et al. A programmable two-qubit quantum processor in silicon. *Nature* **555**, 633 (2018).
16. Zajac, D. M. et al. Resonantly driven CNOT gate for electron spins. *Science* **359**, 439–442 (2018).
17. Jones, C. et al. Logical qubit in a linear array of semiconductor quantum dots. *Phys. Rev. X* **8**, 021058 (2018).
18. Hornibrook, J. M. et al. Cryogenic control architecture for large-scale quantum computing. *Phys. Rev. Appl.* **3**, 024010 (2015).
19. Degenhardt, C., Geck, L., Kruth, A., Vliex, P. & van Waasen, S. CMOS based scalable cryogenic control electronics for qubits. In *Rebooting Computing (ICRC), 2017 IEEE International Conference on*, 1–4 (IEEE, 2017).
20. Veldhorst, M. et al. An addressable quantum dot qubit with fault-tolerant control-fidelity. *Nat. Nanotechnol.* **9**, 981–985 (2014).
21. Maurand, R. et al. A CMOS silicon spin qubit. *Nat. Commun.* **7**, 13575 (2016).
22. Yoneda, J. et al. A quantum-dot spin qubit with coherence limited by charge noise and fidelity higher than 99.9%. *Nat. Nanotechnol.* **13**, 102–106 (2018).
23. Yang, C. H. et al. Silicon qubit fidelities approaching incoherent noise limits via pulse engineering. *Nat. Electron.* **2**, 151–158 (2019).
24. Veldhorst, M. et al. A two-qubit logic gate in silicon. *Nature* **526**, 410–414 (2015).
25. Huang, W. et al. Fidelity benchmarks for two-qubit gates in silicon. *Nature* **569**, 532–536 (2019).
26. Elzerman, J. M. et al. Single-shot read-out of an individual electron spin in a quantum dot. *Nature* **430**, 431 (2004).
27. West, A. et al. Gate-based single-shot readout of spins in silicon. *Nat. Nanotechnol.* **14**, 437–441 (2019).
28. Li, Y. et al. Nanoparticle-laden droplets of liquid crystals: interactive morphogenesis and dynamic assembly. *Sci. Adv.* **5**, eaav1035 (2019).
29. Veldhorst, M. et al. Spin-orbit coupling and operation of multivalley spin qubits. *Phys. Rev. B* **92**, 201401 (2015).
30. Ono, K., Austing, D., Tokura, Y. & Tarucha, S. Current rectification by Pauli exclusion in a weakly coupled double quantum dot system. *Science* **297**, 1313–1317 (2002).
31. Petit, L. et al. Spin lifetime and charge noise in hot silicon quantum dot qubits. *Phys. Rev. Lett.* **121**, 076801 (2018).
32. Shankar, S., Tyryshkin, A. M., He, J. & Lyon, S. A. Spin relaxation and coherence times for electrons at the Si/SiO_2 interface. *Phys. Rev. B* **82**, 195323 (2010).
33. Ono, K., Mori, T. & Moriyama, S. High-temperature operation of a silicon qubit. *Sci. Rep.* **9**, 469 (2019).
34. Tyryshkin, A. M., Lyon, S. A., Astashkin, A. V. & Raitsimring, A. M. Electron spin relaxation times of phosphorus donors in silicon. *Phys. Rev. B* **68**, 193207 (2003).
35. Tyryshkin, A. M. et al. Electron spin coherence exceeding seconds in high-purity silicon. *Nat. Mater.* **11**, 143–147 (2012).
36. Struck, T. et al. Spin relaxation and dephasing in a ^{28}SiGe QD with nanomagnet. *Bull. Am. Phys. Soc.* https://meetings.aps.org/Meeting/MAR19/Session/B35.9 (2019).
37. Witzel, W. M., Carroll, M. S., Morello, A., Cywiński, Ł. & Sarma, S. D. Electron spin decoherence in isotope-enriched silicon. *Phys. Rev. Lett.* **105**, 187602 (2010).
38. Urdampilleta, M. et al. Gate-based high fidelity spin readout in a CMOS device. *Nat. Nanotechnol.* **14**, 737–741 (2019).

Methods

Feedback controls

The following three types of feedback/calibration processes are implemented for the experiments.

SET sensor current feedback. For each current trace acquired by the digitizer, the I_{SET} value during the 'reset' stage is compared against a set value. In Fig. 2a, this set value is 50 pA. The SET top-gate voltage is then adjusted to ensure I_{SET} stays at ~50 pA.

Charge detuning feedback. The charge detuning level between the two dots is controlled by monitoring the bias at which the charge transition occurs, shown by the red arrow in Fig. 2a. By adjusting the bias on V_{G1}, the charge transition is then retuned to occur at 60% of the 'read feedback' stage.

Spin qubit resonance calibration. Frequency calibration of the microwave frequencies is applied during the measurement shown in Fig. 3d, h. The calibration protocol is the same as the one detailed in ref. [25].

Temperature control

For operation at base temperature $T_{MC} = 40$ mK, the circulation of ^{3}He is fully enabled. For $T_{MC} > 40$ mK and $T_{MC} \leq 1$ K, we turn on the heater at the mixing chamber stage (see Extended Data Fig. 1) with a proportional integral computer controller. For $T_{MC} = 1.5$ K, the ^{3}He circulation is completely stopped by closing the circulation valves and turning off all heaters. The fridge is then left for at least one day for T_{MC} to saturate at 1.5 K, the temperature of the 1-K pot stage. The 1-K pot is actively pumped during all the measurements in this work.

To validate the accuracy of the temperature measurement, we perform effective electron temperature measurements of the isolated QDs by measuring the broadening of the (2, 4)–(3, 3) charge transition as shown in Extended Data Fig. 6a. Having determined the lever arms from magnetospectroscopy (see Extended Data Fig. 7), we fit the charge transitions to extract the effective electron temperatures (see Extended Data Fig. 6b). For $T_{MC} > 0.4$ K, the extracted temperature matches well with the mixing chamber thermometer of the fridge.

Ramsey measurement of wait-time-dependent phase

To extract T_2^* times at high temperatures, where the control pulses are of similar duration as the coherence time, the conventional way of setting a resonance frequency detuning would greatly suppress the already low visibility of the oscillations. A more efficient way to extract T_2^* is to use zero-detuning pulses while applying a large wait-time-dependent phase shift to the second π/2 pulse. This results in fast Ramsey fringes while maintaining maximum visibility. For example, in Fig. 3g, the phase of the second microwave pulse has the dependency $\theta_{MW} = 2 \times 10^6 \times 2\pi\tau_{wait}$, giving Ramsey fringes with a frequency of 2 MHz.

For all Ramsey measurements, each data point consists of 100 single shots per acquisition, with five overall repeats, giving a total of 500 single shots.

Parity readout

In general, the joint state of a pair of spins may be measured through a spin-to-charge conversion based on the Pauli exclusion principle. In a double-dot system, interdot tunnelling is stimulated by detuning the energy levels of one QD with respect to the other. If the pair of electrons is in the singlet state, tunnelling will occur, and the charge distribution in the double dot will change. A charge measurement then allows us to distinguish a singlet state from any one of the spin triplets.

For simplicity, we refer to the possible charge configurations as (1, 1) → (0, 2), but any configuration with two effective valence spins is valid, including the (3, 3) charge configuration investigated here. If Pauli spin blockade occurred in the standard way, we would have the simple mapping

$$|(1,1)\mathrm{S}\rangle \rightarrow |(0,2)\mathrm{S}\rangle \quad (1)$$

$$|(1,1)\mathrm{T}_0\rangle \rightarrow |(1,1)\mathrm{T}_0\rangle \quad (2)$$

$$|(1,1)\mathrm{T}_+\rangle \rightarrow |(1,1)\mathrm{T}_+\rangle \quad (3)$$

$$|(1,1)\mathrm{T}_-\rangle \rightarrow |(1,1)\mathrm{T}_-\rangle \quad (4)$$

and the final state after the measurement would be a pure state. A measurement of the charge state would distinguish singlets from triplets, that is, discern between distinct eigenstates of total angular momentum $\hat{S}^2_{TOT} = (\hat{S}_1 + \hat{S}_2)^2$.

In practice, relaxation between the triplet states and the singlet ground state occurs at the same time as the charge measurement process. Spin-flip relaxation is slower than 10 ms for all temperatures studied here, as shown in Fig. 4, so the T_+ and T_- states will be preserved for a sufficiently long time for our SET-based measurement to be completed.

On the other hand, the T_0 triplet and the singlet are constantly mixing with each other, either through the difference in Overhauser fields from nuclear spins (reduced here in isotopically enriched ^{28}Si), the difference in g-factors under the applied external magnetic field, or because of the field gradient of the micromagnet.

The wavefunction component of $|(1,1)\mathrm{T}_0\rangle$ that mixes into the $|(1,1)\mathrm{S}\rangle$ state rapidly relaxes into the $|(0,2)\mathrm{S}\rangle$ state. This means that at the timescale of the S–T_0 mixing, the population in $|(1,1)\mathrm{T}_0\rangle$ is depleted and relaxes into $|(0,2)\mathrm{S}\rangle$.

Because this relaxation mechanism is much faster than any spin-flip mechanism, after a sufficiently long time (compared to the S–T_0 mixing rate and the tunnel/charge relaxation rate), the T_0 state has completely relaxed into the singlet state, and the mapping connects again two pure states

$$|(1,1)\mathrm{S}\rangle \rightarrow |(0,2)\mathrm{S}\rangle \quad (5)$$

$$|(1,1)\mathrm{T}_0\rangle \rightarrow |(0,2)\mathrm{S}\rangle \quad (6)$$

$$|(1,1)\mathrm{T}_+\rangle \rightarrow |(1,1)\mathrm{T}_+\rangle \quad (7)$$

$$|(1,1)\mathrm{T}_-\rangle \rightarrow |(1,1)\mathrm{T}_-\rangle \quad (8)$$

Now, a charge measurement can distinguish between states of parallel or anti-parallel spins, represented by the observable $\hat{P}_{ZZ} = \frac{1}{2}(\hat{\sigma}_{\mathrm{II}} - \hat{\sigma}_{ZZ})$ This measurement therefore corresponds to a parity readout.

The proposal by Veldhorst et al.[8] on the implementation of a CMOS-based, scalable quantum computer, describes how parity readout can be directly integrated within error detection and correction codes, such as the surface code. To facilitate this, the unit cell in the surface code contains two data qubits and four measurement qubits, instead of the usual two data and two measurement qubits. Here, data qubits do not require any direct state initialization and readout, and a pair of QDs, as in our unit cell, serves as a measurement ancilla. The pair is measured via parity readout, and its parity will remain unaffected by the measurement, given that the readout time is much shorter than the parity time T_1.

Confirming initializations using spin relaxation

By preparing a $|\downarrow\downarrow\rangle$ state, we measure the spin relaxation time T_1 for both qubits by selectively flipping one of them to a spin-up state, followed by a wait time, τ_{wait}. Extended Data Fig. 4a–c is fitted using a simple decay equation, $A\exp(-\tau_{wait}/T_1) + C$, when driving Q_1 to spin-up

(Extended Data Fig. 4a), for off-resonance drive (Extended Data Fig. 4b), and Q_2 to spin-up (Extended Data Fig. 4c). The two qubits have $T_1 = 540$ ms and 36 ms, respectively.

When we repeat the same measurement with a S-like initialization, we observe a mixed decay pattern. We now need to fit to a more complicated equation that measures the parity of the spins while both spins are relaxing, assuming no knowledge of the initial state.

For $|\uparrow\downarrow\rangle$ and $|\downarrow\uparrow\rangle$ components, the relaxation equations for parity readout are

$$P_{ZZ|\uparrow\downarrow\rangle} = A_{|\uparrow\downarrow\rangle} e_1 + C \tag{9}$$

$$P_{ZZ|\downarrow\uparrow\rangle} = A_{|\downarrow\uparrow\rangle} e_2 + C \tag{10}$$

where

$$e_1 = \exp\left(-\tau_{\text{wait}}/T_{1Q1}\right) \tag{11}$$

$$e_2 = \exp\left(-\tau_{\text{wait}}/T_{1Q2}\right) \tag{12}$$

For a $|\uparrow\uparrow\rangle$ component, assuming no two-spin interactions, it is then

$$P_{ZZ|\uparrow\uparrow\rangle} = -2A_{|\uparrow\uparrow\rangle}\left(e_1 - \frac{1}{2}\right)\left(e_2 - \frac{1}{2}\right) + \frac{1}{2} + C \tag{13}$$

By combining equations (9), (10) and (13), for an arbitrary initial-state fitting we obtain

$$P_{ZZ} = \left(A_{|\uparrow\uparrow\rangle} + A_{|\uparrow\downarrow\rangle}\right)e_1 + \left(A_{|\uparrow\uparrow\rangle} + A_{|\downarrow\uparrow\rangle}\right)e_2 - 2A_{|\uparrow\uparrow\rangle}e_1e_2 + C \tag{14}$$

Equation (14) is then applied to fit Extended Data Fig. 4d–f, which then gives the probability of each eigenstate for S-like initialization, proving that indeed it is an equal mixture of $|\uparrow\downarrow\rangle$ and $|\downarrow\uparrow\rangle$ states.

Data availability

The datasets generated and/or analysed during this study are available from the corresponding authors on reasonable request.

Code availability

The analysis codes that support the findings of the study are available from the corresponding authors on reasonable request.

39. Angus, S. J., Ferguson, A. J., Dzurak, A. S. & Clark, R. G. Gate-defined quantum dots in intrinsic silicon. *Nano Lett.* **7**, 2051–2055 (2007).
40. Lim, W. H. et al. Observation of the single-electron regime in a highly tunable silicon quantum dot. *Appl. Phys. Lett.* **95**, 242102 (2009).
41. Medford, J. et al. Self-consistent measurement and state tomography of an exchange-only spin qubit. *Nat. Nanotechnol.* **8**, 654 (2013).

Acknowledgements We acknowledge support from the US Army Research Office (W911NF-17-1-0198), the Australian Research Council (CE170100012), Silicon Quantum Computing Proprietary Limited and the NSW Node of the Australian National Fabrication Facility. The views and conclusions contained in this document are those of the authors and should not be interpreted as representing the official policies, either expressed or implied, of the Army Research Office or the US Government. The US Government is authorized to reproduce and distribute reprints for Government purposes notwithstanding any copyright notation herein. K.M.I. acknowledges support from a Grant-in-Aid for Scientific Research by MEXT. J.C.L. and M.P.-L. acknowledge support from the Canada First Research Excellence Fund and in part by the National Science Engineering Research Council of Canada. K.Y.T. acknowledges support from the Academy of Finland through projects 308161, 314302 and 316551. This work was funded in part by Silicon Quantum Computing Proprietary Limited.

Author contributions C.H.Y. designed and performed the experiments. C.H.Y., R.C.C.L. and A.S. analysed the data. J.C.C.H. and F.E.H. fabricated the device under A.S.D.'s supervision. J.C.C.H., T.T. and W.H. contributed to the preparation of the experiments. J.C.L., R.C.C.L., J.C.C.H., C.H.Y. and M.P.-L. designed the device. K.W.C. and K.Y.T. contributed to discussions on the nanofabrication process. K.M.I. prepared and supplied the ^{28}Si epilayer. T.T., W.H., A.M. and A.L. contributed to the discussion and interpretation of the results. C.H.Y., A.S., A.L. and A.S.D. wrote the manuscript with input from all co-authors.

Competing interests The authors declare no competing interests.

Additional information
Correspondence and requests for materials should be addressed to C.H.Y. or A.S.D.
Peer review information *Nature* thanks John Gamble, HongWen Jiang and the other, anonymous, reviewer(s) for their contribution to the peer review of this work.

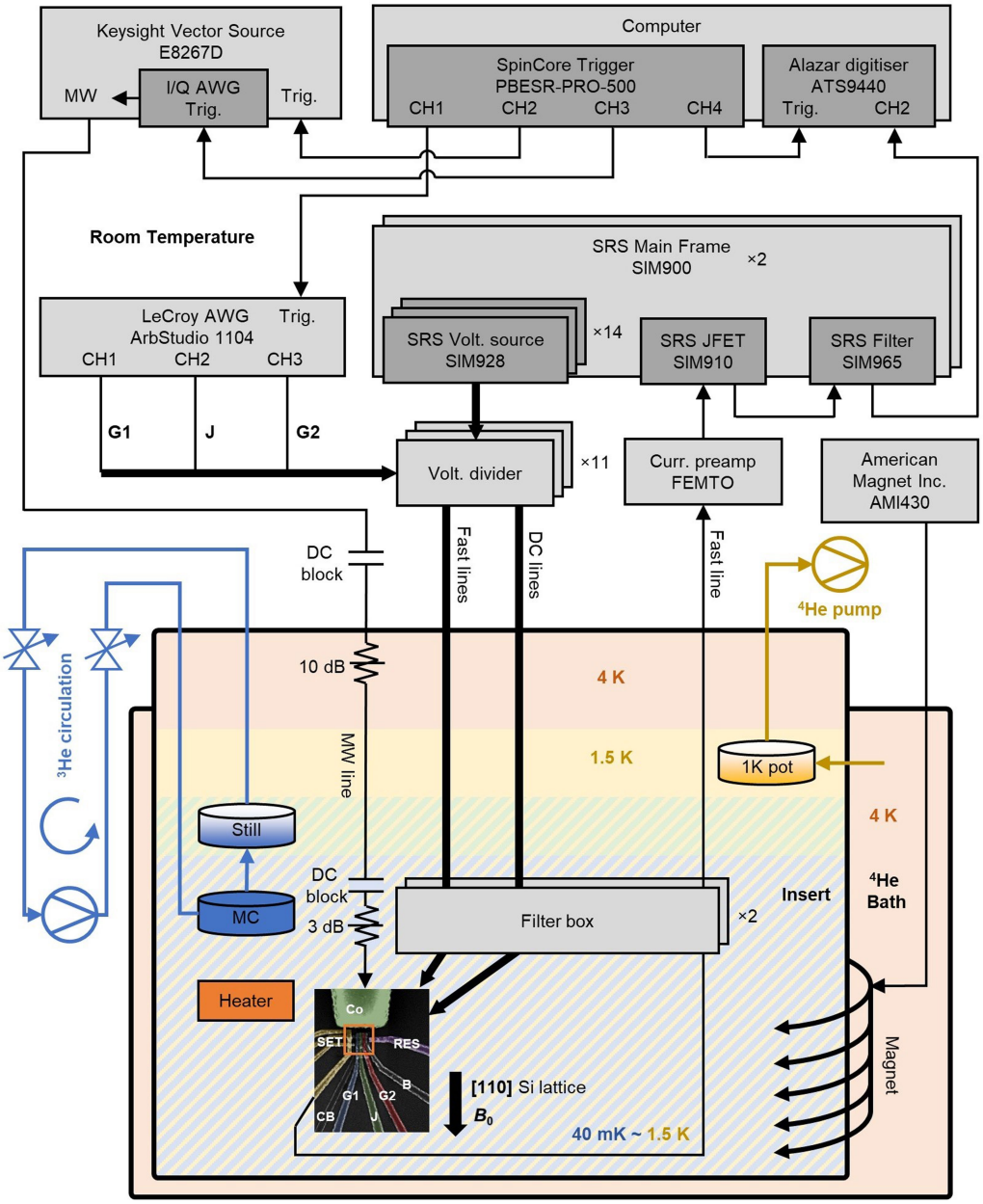

Extended Data Fig. 1 | Experimental setup. The device measured is identical to the one described in ref. [11]. It is fabricated on an isotopically enriched 900-nm-thick ^{28}Si epilayer[12] with 800 ppm residual concentration of ^{29}Si using multi-layer gate-stack silicon MOS technology[39,40]. Rechargeable isolated voltage source modules (SIM928 from Stanford Research System, SRS, mounted in SRS SIM900 mainframes) are used to supply all our d.c. (DC) voltages, and a LeCroy ArbStudio 1104 arbitrary waveform generator (AWG) is combined with the d.c. voltages through resistive voltage dividers, with 1/5 division for the d.c. and 1/25 for the AWG inputs. The resistance of the voltage dividers in combination with the capacitance of the coaxial cables limits the AWG bandwidth to ~5 MHz. Filter boxes with lowpass filtering (100 Hz for d.c. lines and 80 MHz for fast lines) and thermalization are mounted on the mixing chamber (MC) plate. Shaped microwave (MW) pulses are delivered by an Agilent E8267D vector signal generator, employing its own internal AWG for in-phase/quadrature (IQ) modulation. There are two d.c. blocks and two attenuators along the microwave line, as indicated in the schematic. The SET sensor current signal is amplified by a FEMTO DLPCA-200 transimpedance amplifier and an SRS SIM910 JFET isolation amplifier with gain of 100, before passing an SRS SIM965 lowpass filter and finally being acquired by an Alazar ATS9440 digitizer. The SpinCore PBESR-PRO-500 pulse generator acts as the master trigger source for all other instruments. The device sits inside an Oxford Kelvinox 100 wet dilution refrigerator with base temperature T_{MC} = 40 mK. The superconducting magnet is powered by an American Magnet Inc. AMI430 power supply. CH1–CH4, physical channel input/output 1–4 from the instruments.

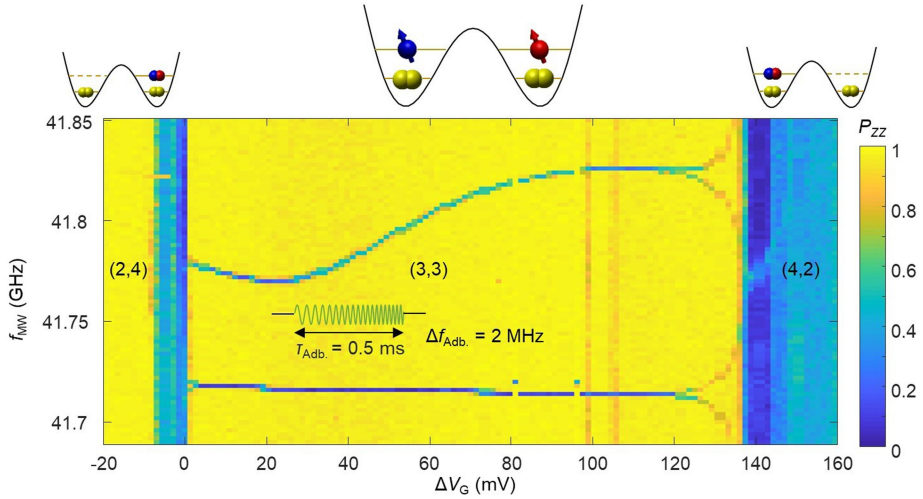

Extended Data Fig. 2 | Qubit spectra in the (3, 3) charge configuration region. EDSR spectra of Q_1 (lower frequency) and Q_2 (upper frequency) as a function of $\Delta V_G = V_{G1} - V_{G2}$, measured using adiabatic microwave pulses with frequency sweep range $\Delta f_{Adb} = 2$ MHz and pulse time $\tau_{Adb} = 2$ MHz, at $B_0 = 1.4$ T and $T_{MC} = 40$ mK. The cobalt magnet is designed to minimize the magnetic field difference between the two QDs. The bending of the spectrum of Q_2 suggests strong mixing with an excited state. Near the (4, 2) region, both spectra split up equally owing to the increase of J coupling. A small splitting can also been seen near the (2, 4) region. At the (2, 4) and (4, 2) electron charge transitions, we no longer have a proper effective two-spin system and the signal vanishes. We operate our qubits mostly near the (2, 4) side (left) for faster EDSR control over Q_1.

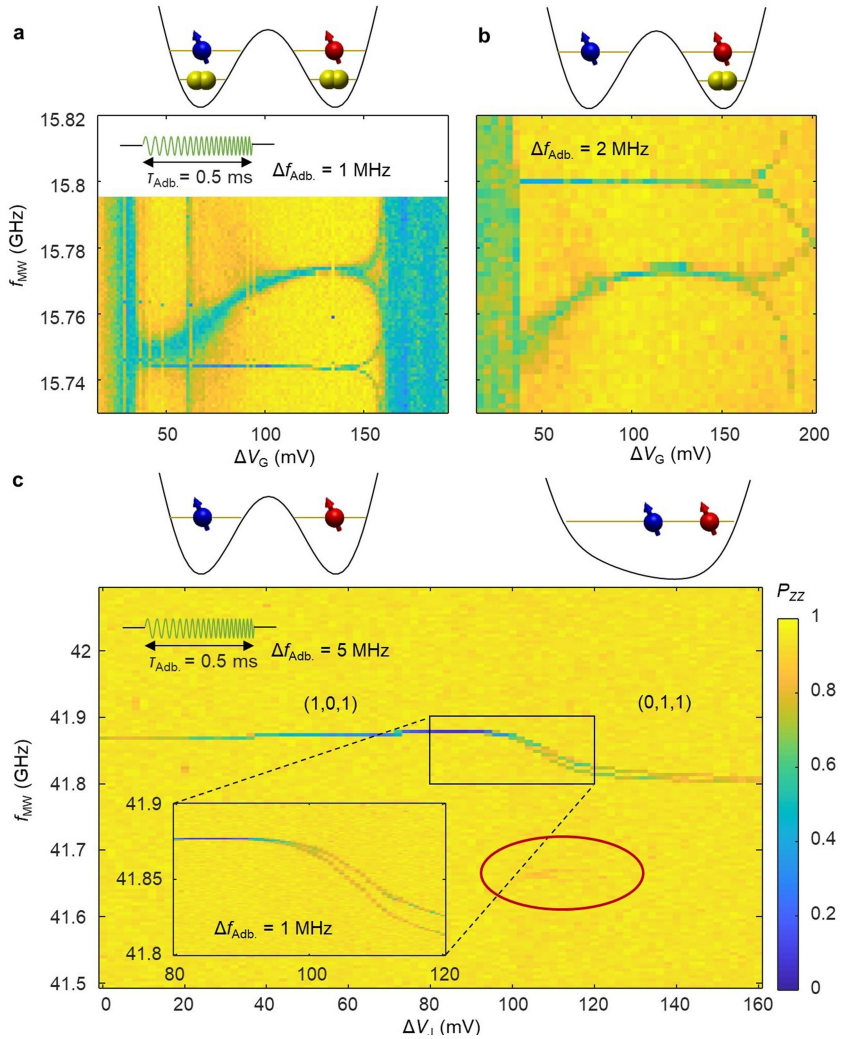

Extended Data Fig. 3 | Qubit spectra in other charge configurations. **a**, **b**, EDSR spectra of the (3, 3) (**a**) and (1, 3) (**b**) charge configurations as a function of $\Delta V_G = V_{G1} - V_{G2}$ at $B_0 = 0.5$ T and $T_{MC} = 40$ mK. Between (3, 3) and (1, 3), the number of electrons in Q_1 changes, but it remains constant in Q_2. Whereas the bending spectrum exhibits minimal change in frequency and can be attributed to Q_2, the straight spectrum shifts by more than 50 MHz, confirming that it corresponds to Q_1. The large change in the frequency of Q_1 is mainly due to the unpaired-electron spin now occupying the other valley state. **c**, For large V_J, a third QD starts forming under the J gate (compare with Fig. 1), and the device can be operated as a two-qubit system with two electrons in the (1, 0, 1) and (0, 1, 1) configurations at $B_0 = 1.4$ T and $T_{MC} = 40$ mK. Only one qubit resonance is clearly found, whereas the other one is only weakly observed when J coupling increases (red circle), where spin–orbit coupling is stronger for the tightly confined dot. Inset, J coupling increases with V_J, demonstrating control of J when moving one electron from the (1, 0, 1) to the (0, 1, 1) charge configuration.

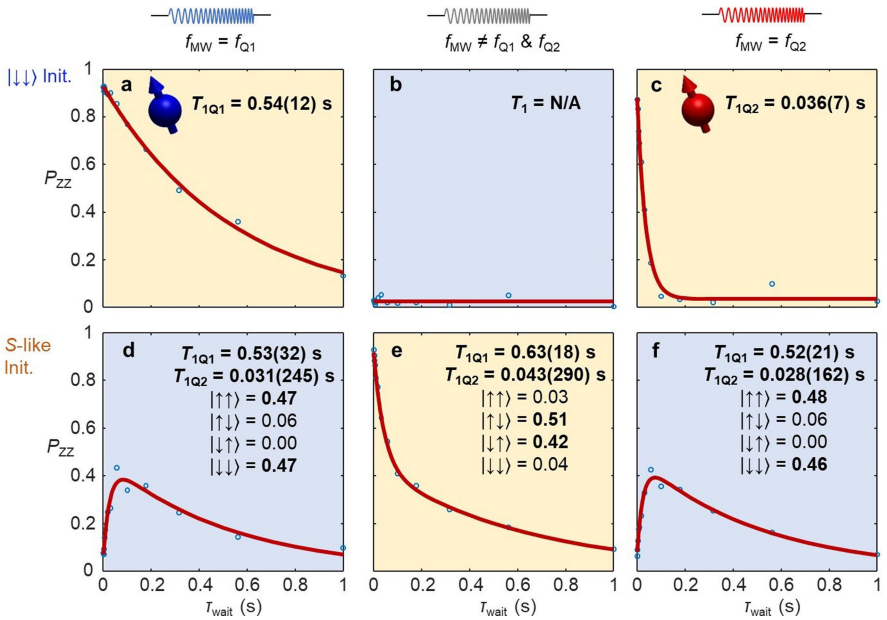

Extended Data Fig. 4 | Spin relaxation measurements using parity readout. **a**–**c**, P_{ZZ} with $|{\downarrow\downarrow}\rangle$ initialization and flipping the spin of Q_1 adiabatically via EDSR ($|{\uparrow\downarrow}\rangle$) (**a**), no spin flip ($|{\downarrow\downarrow}\rangle$) (**b**) and flipping the spin of Q_2 adiabatically ($|{\downarrow\uparrow}\rangle$) (**c**). **d**–**f**, P_{ZZ} with S-like initialization and flipping the spin of Q_1 adiabatically (**d**), no spin flip (**e**) and flipping the spin of Q_2 adiabatically via EDSR (**f**). The measurements were performed at $B_0 = 1.4$ T and $T_{MC} = 40$ mK. Each data point is the average of 100 single shots, with three overall repeats, giving a total of 300 single shots. All fits are according to equations (9)–(14). The error range of T_1 represents the 95% confidence level.

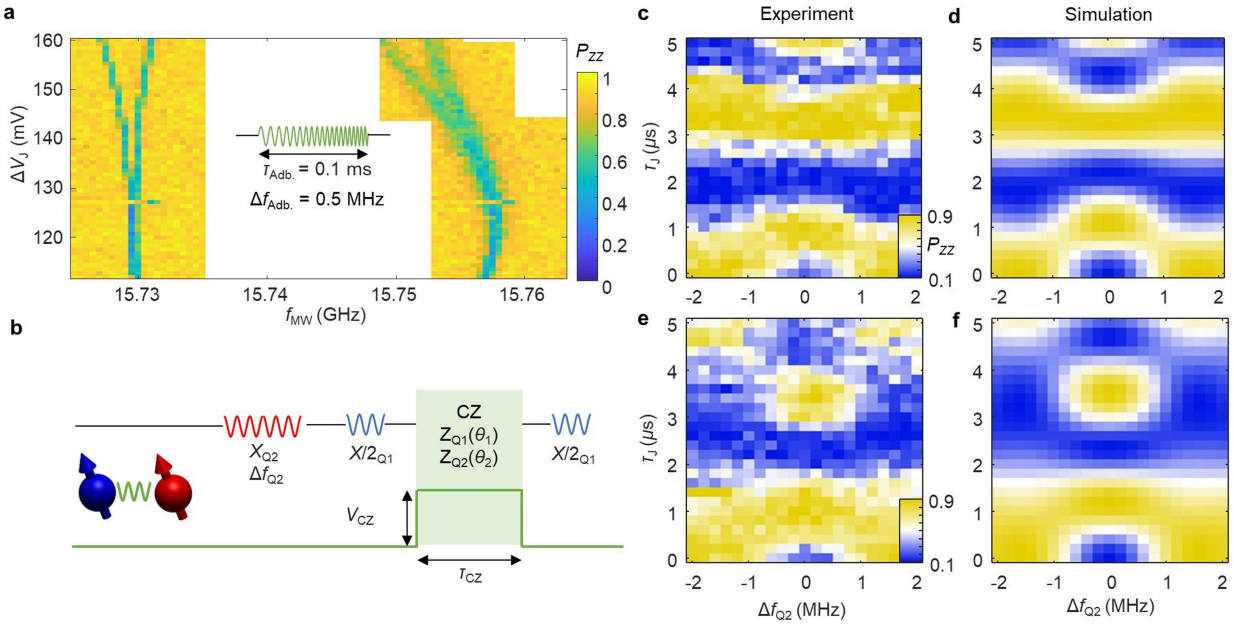

Extended Data Fig. 5 | CNOT operation via exchange gate pulsing. Data measured at $B_0 = 0.8$ T and $T_{MC} = 40$ mK. **a**, EDSR spectra of Q_1 and Q_2 as a function of voltage ΔV_J applied to gate J. At large ΔV_J, the resonance lines clearly split, demonstrating control over the J coupling. **b**, Pulse sequence of a CNOT-like two-qubit gate. **c**, **d**, Measured and simulated parity readout (P_{ZZ}) after applying the pulse sequence in **b**, as a function of Δf_{Q2} and exchange pulse time τ_J, for $V_{CZ} = 30$ mV. Here, V_{G1} is also pulsed at 20% of V_{CZ} to maintain a constant charge detuning. The CZ fidelity is >90%, as confirmed by observing no substantial decay over four CZ cycles. The simulated Hamiltonian uses a σ_{ZI} coefficient of 370 kHz and a σ_{ZZ} coefficient of 89 kHz. The good agreement with the experimental data validates the performance of the CNOT gate. **e**, **f**, As in **c**, **d**, but with $V_{CZ} = 32$ mV. The simulated Hamiltonian has a σ_{ZI} coefficient of 290 kHz and a σ_{ZZ} coefficient of 135 kHz. Small charge rearrangement occurs in the device between **c** and **e**.

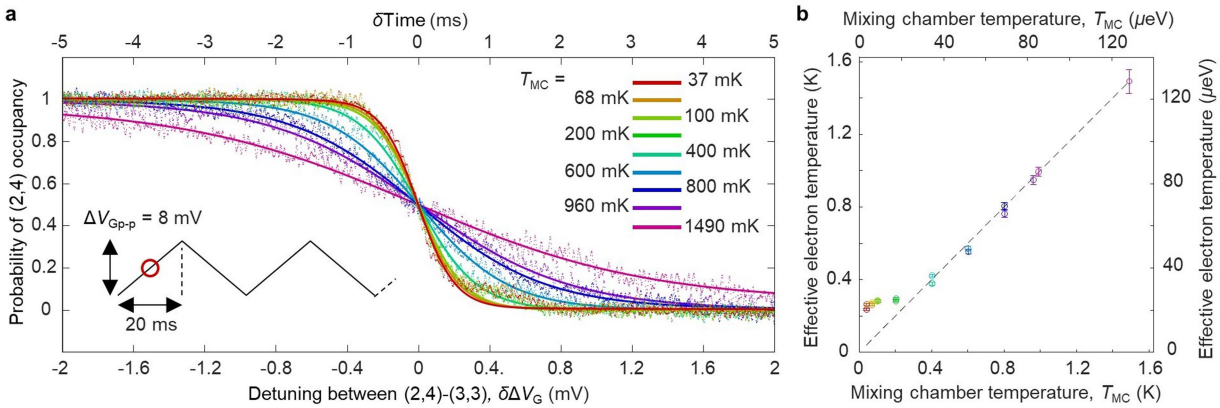

Extended Data Fig. 6 | Effective electron temperature of the isolated QD unit cell. a, Charge occupation probability around the (2, 4)–(3, 3) charge transition, measured through I_{SET} using a triangular wave with a peak-to-peak voltage of ΔV_{Gp-p} = 8 mV applied to ΔV_G. $\delta\Delta V_G$ is the rebiased ΔV_G value for which the fitted charge transitions occur at 0 V. The solid lines are fits to the Fermi distribution, which we use to extract the effective electron temperature as a function of mixing chamber temperature. **b**, Effective electron temperatures extracted from **a**. The effective temperature is calculated using the lever arm from Extended Data Fig. 7. The minimum effective electron temperature is ~250 mK at low mixing chamber temperatures. At higher temperatures, the effective electron temperature is equal to the mixing chamber temperature. Measured at B_0 = 0 T. Error bars represent the 95% confidence level.

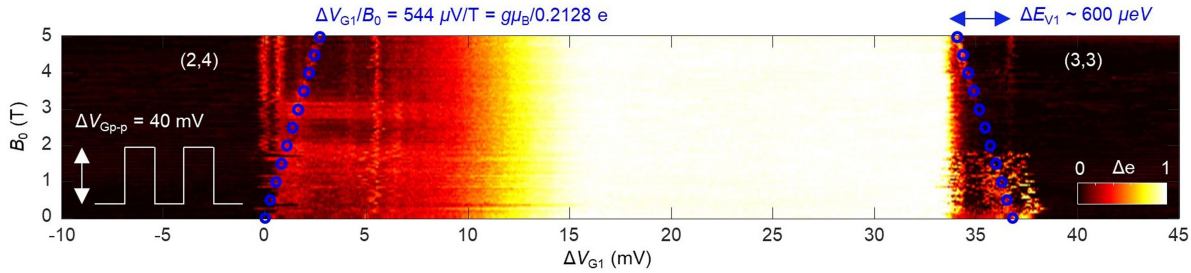

Extended Data Fig. 7 | Magnetospectroscopy of the (2, 4) and (3, 3) charge configurations. The transitions that move with the magnetic field are caused by Zeeman splitting, allowing us to extract the lever arm of V_{G1} as 0.2128. Because $\Delta V_{Gp-p} = \Delta V_{G1} - \Delta V_{G3}$, and the pulse is applied symmetrically to both G_1 and G_3, we can further extract the lever arm of V_{G3} to be $0.2128 \times \frac{36.8\ \text{mV} - 20\ \text{mV}}{40\ \text{mV} - 20\ \text{mV}} = 0.1788$. The valley splitting energy of the QDs can be approximated as 600 μeV, where the blockaded region at (3, 3) corresponds to the splitting energy. Further evidence can be found in ref. [11], where no valley splitting below 600 μeV was observed in the low-electron-number regime for this same QD device. g, g-factor of electron in silicon ($g = 2$); μ_B, Bohr magneton; e, electron charge; ΔE_{V1}, valley splitting energy of QD_1.

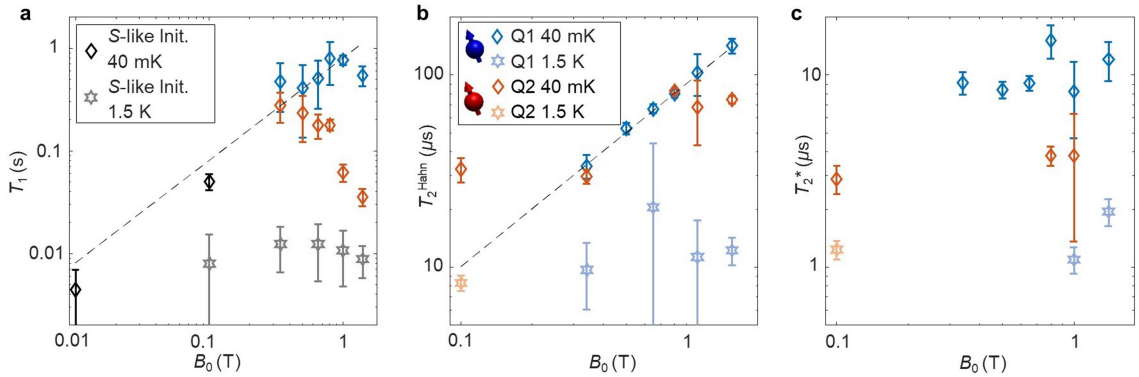

Extended Data Fig. 8 | Magnetic field dependence of qubit properties. a–c, Spin relaxation time T_1 (**a**), Hahn Echo coherence time T_2^{Hahn} (**b**) and Ramsey coherence time T_2^* (**c**) as a function of external magnetic field B_0. Error bars represent the 95% confidence level.

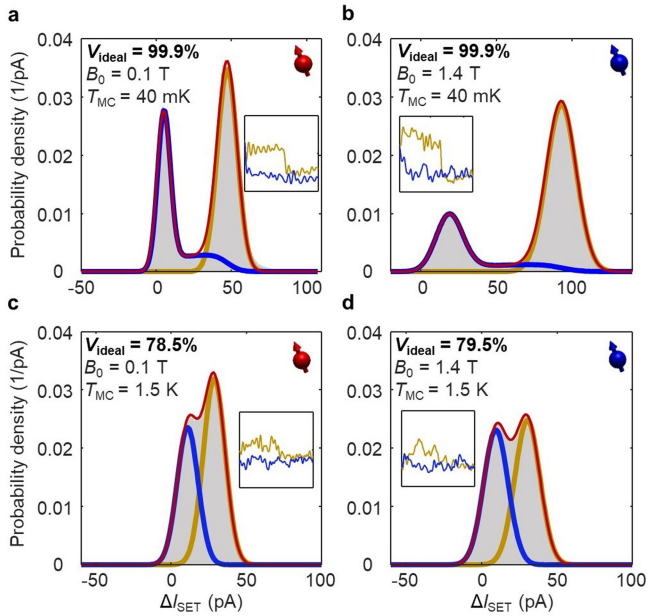

Extended Data Fig. 9 | Readout visibility of the SET charge sensor. **a**–**d**, Histograms of the charge sensor current $\Delta I_{SET} = \bar{I}_{SET}(\text{read}) - \bar{I}_{SET}(\text{reset})$ for Fig. 3a (**a**; $T_{MC} = 40$ mK, $B_0 = 0.1$ T), Fig. 3b (**b**; $T_{MC} = 40$ mK, $B_0 = 1.4$ T), Fig. 3e (**c**; $T_{MC} = 1.5$ K, $B_0 = 0.1$ T) and Fig. 3f (**d**; $T_{MC} = 1.5$ K, $B_0 = 1.4$ T). The histograms in **a**, **b** are fitted with a Gaussian model including decay from the even-parity state to the odd-parity state during the readout period[41]. The extracted visibilities are 88.1% (**a**) and 89.3% (**b**). Assuming no state decay during readout, the ideal readout visibility, which corresponds to the charge readout visibility, would be $V_{ideal} = 99.9\%$ for $T_{MC} = 40$ mK. The histograms in **c**, **d** are fitted to the ideal Gaussian model only, giving $V_{ideal} = 78.5\%$ and $V_{ideal} = 79.5\%$ for $T_{MC} = 1.5$ K. This clearly highlights the limitations of SET charge sensing at increased temperatures, owing to the thermal distribution of electrons in the SET source and drain reservoirs. The insets show example I_{SET} traces for odd- and even-parity state readout, with the horizontal axis showing the time from 0.2 µs to 4.5 µs, the vertical axis showing the current up to 200 pA (arbitrarily shifted), and a measurement bandwidth of 3 kHz .

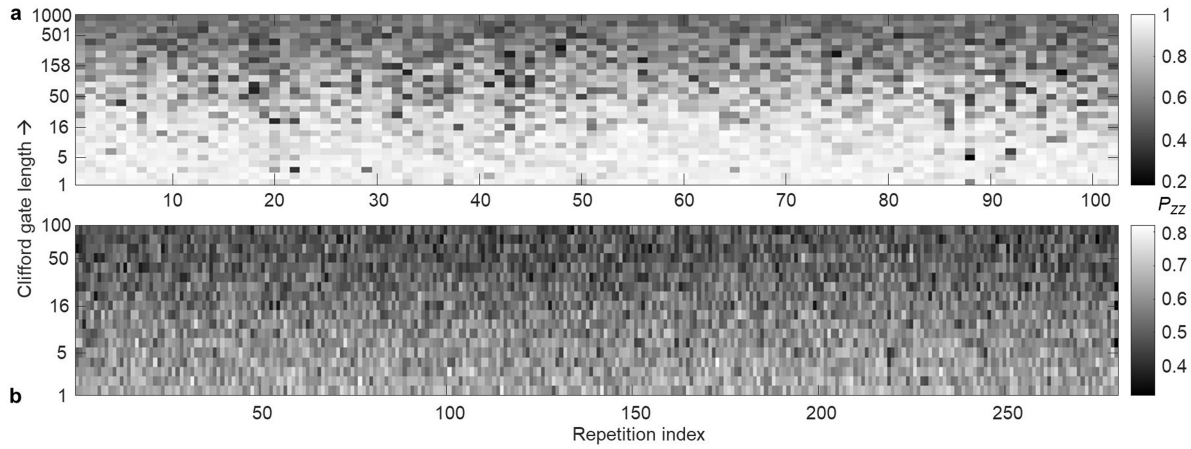

Extended Data Fig. 10 | Expanded randomized benchmarking data. **a**, Complete datasets of the randomized benchmarking data in Fig. 3d, with a total of 102 repetitions of a randomized sequence, with Clifford gate lengths {1, 2, 3, 4, 5, 6, 8, 10, 13, 16, 20, 25, 32, 40, 50, 63, 79, 100, 126, 158, 200, 251, 316, 398, 501, 631, 794, 1,000}. **b**, Complete datasets of the randomized benchmarking data in Fig. 3h, with a total of 280 repetitions of a randomized sequence, with Clifford gate lengths {1, 2, 3, 4, 5, 6, 8, 10, 13, 16, 20, 25, 32, 40, 50, 63, 79, 100}.

Author Queries

Journal: **Nature**
Paper: **s41586-020-2171-6**
Title:**Operation of a silicon quantum processor unit cell above one kelvin**

AUTHOR:
The following queries have arisen during the editing of your manuscript. Please answer by making the requisite corrections directly in the e.proofing tool rather than marking them up on the PDF. This will ensure that your corrections are incorporated accurately and that your paper is published as quickly as possible.

Query Reference	Reference
Q1	Please check that the display items are as follows (ms no: 2019-06-09217): Figs 4 (colour); Tables: None; Boxes: None; Extended Data display items: 10 figures; SI: none. The eproof contains the main-text figures edited by us and and the Extended Data items (unedited except for the legends). Please check the edits to all main-text figures very carefully, and ensure that any error bars in the figures are defined in the figure legends. Extended Data items may be revised only if there are errors in the original submissions.
Q2	Please check your article carefully, coordinate with any co-authors and enter all final edits clearly in the eproof, remembering to save frequently. Once corrections are submitted, we cannot routinely make further changes to the article.
Q3	Note that the eproof should be amended in only one browser window at any one time; otherwise changes will be overwritten.
Q4	Author surnames have been highlighted. Please check these carefully and adjust if the first name or surname is marked up incorrectly. Note that changes here will affect indexing of your article in public repositories such as PubMed. Also, carefully check the spelling and numbering of all author names and affiliations, and the corresponding email address(es).
Q5	You cannot alter accepted Supplementary Information files except for critical changes to scientific content. If you do resupply any files, please also provide a brief (but complete) list of changes. If these are not considered scientific changes, any altered Supplementary files will not be used, only the originally accepted version will be published.
Q6	If ref. 4 (preprint) has now been published in final peer-reviewed form, please update the reference details if appropriate.